JGR Space Physics

RESEARCH ARTICLE
10.1029/2020JA027973

Particle Simulation of the Generation of Plasmaspheric Hiss

Mitsuru Hikishima[1], Yoshiharu Omura[2], and Danny Summers[3]

[1]Institute of Space and Astronautical Science, Japan Aerospace Exploration Agency, Sagamihara, Japan, [2]Research Institute for Sustainable Humanosphere, Kyoto University, Kyoto, Japan, [3]Department of Mathematics and Statistics, Memorial University of Newfoundland, St. John's, Newfoundland and Labrador, Canada

Key Points:

- PIC simulation demonstrates that plasmaspheric hiss is generated locally near the magnetic equator
- Hiss emissions have fine structure growing from thermal fluctuations through linear and nonlinear wave growth processes
- Electrons are efficiently scattered by coherent hiss emissions into the loss cone

Correspondence to:
M. Hikishima,
mitsuru.hikishima@gmail.com

Citation:
Hikishima, M., Omura, Y., & Summers, D. (2020). Particle simulation of the generation of plasmaspheric hiss. *Journal of Geophysical Research: Space Physics*, *125*, e2020JA027973. https://doi.org/10.1029/2020JA027973

Received 4 MAR 2020
Accepted 9 JUN 2020
Accepted article online 7 JUL 2020

Abstract We have conducted a one-dimensional electromagnetic particle simulation with a parabolic magnetic field to reproduce whistler-mode hiss emissions in the plasmasphere. We assume a bi-Maxwellian distribution with temperature anisotropy for energetic electrons injected into the plasmasphere and find that hiss emissions are generated with spectrum characteristics typical of those observed by spacecraft near the magnetic equator. The hiss emissions contain fine structures involving rising tone and falling tone elements with variation in frequencies. The amplitude profile of the spectra agrees with the optimum wave amplitude derived from the nonlinear wave growth theory. The simulation demonstrates that hiss emissions are generated locally near the magnetic equator through linear and nonlinear interactions with energetic electrons with temperature anisotropy. The coherent hiss emissions efficiently scatter resonant electrons of 2.5–80 keV into the loss cone.

1. Introduction

Whistler-mode hiss is a commonly occurring electromagnetic emission in the Earth's plasmasphere and plasmaspheric plumes. Dependent on local magnetic conditions, typical hiss frequencies range from ~100 Hz to several kHz, and amplitudes range from a few pT to hundreds of pT. There have been extensive observations of hiss dating from the earlier years of the satellite age to the present day (e.g., Hartley et al., 2018; He et al., 2019; Kim & Shprits, 2019; Li et al., 2013; Liu et al., 2020; Malaspina et al., 2017; Meredith et al., 2004, 2018; Nakamura et al., 2016, 2018; Ni et al., 2014; Smith et al., 1974; Su et al., 2018; Summers et al., 2008, 2014; Thorne et al., 1973, 1974, 1977; Tsurutani et al., 1975, 2015, 2018). Dependent on the location of the plasmapause and plasmaspheric plumes, hiss can efficiently pitch-angle scatter electrons in the energy range from ~10 keV to several MeV over all magnetic local time and the nominal L-shell range, $1<L<7$. Thus, hiss is a primary agent for influencing the distribution and dynamics of electrons throughout the inner magnetosphere (e.g., Breneman et al., 2015; Li et al., 2014; Meredith et al., 2006; Ni et al., 2014; Summers et al., 2007a, 2007b; Thorne et al., 2013; Tsurutani et al., 1975; Zhang et al., 2018). In fact, cyclotron resonant pitch-angle scattering by plasmaspheric hiss is considered responsible for the formation of the "slot region" (approximately $2.5 < L < 3$) between the inner and outer electron radiation belts (Lyons & Thorne, 1973; Lyons et al., 1972).

The primary excitation mechanism of plasmaspheric hiss appears to be electron cyclotron resonance resulting from the injection of a distribution of anisotropic electrons into the magnetic equatorial plane. This generation mechanism for hiss was originally suggested in the early studies (e.g., Kennel & Petschek, 1966; Kennel & Thorne, 1967; Thorne et al., 1979); see also the more recent work by Cornilleau-Wehrlin et al. (1993), He et al. (2019), Kletzing et al. (2014), and Su et al. (2018). It is possible that lightning may also excite plasmaspheric hiss at frequencies of several kHz (e.g., Green et al., 2005). Bortnik et al. (2008) suggested a novel mechanism whereby distinct chorus waves originating outside the plasmasphere could propagate into the plasmasphere and evolve into hiss. However, Hartley et al. (2019), using observations from the Electric and Magnetic Field Instrument Suite and Integrated Science (EMFISIS) instrument on the Van Allen Probes, together with ray tracing simulations, find it unlikely that chorus could contribute significantly to plasmaspheric hiss wave power.

The study by Summers et al. (2014) was the first to identify and examine the fine structure of plasmaspheric hiss. Using waveform burst data from the EMFISIS instrument on eight 1 s samples, Summers et al. (2014)

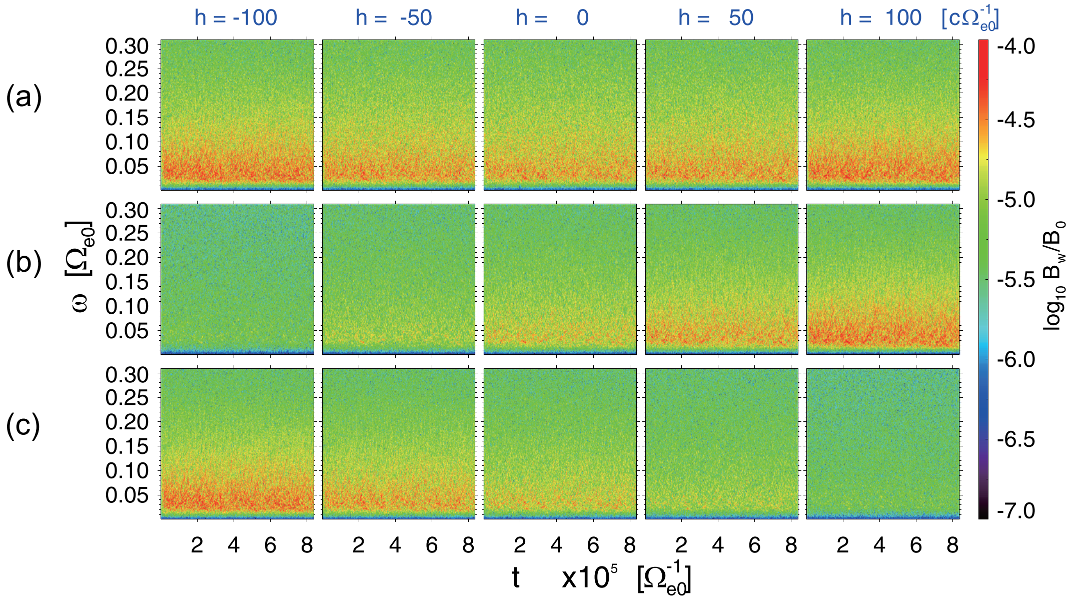

Figure 1. (a) Frequency-time spectrograms (ω–t) of transverse wave magnetic field B_w during the period $t = 0$–8×10^5 Ω_{e0}^{-1} at different locations $h = -100,-50,0,50,100\,c\Omega_{e0}^{-1}$ along the ambient magnetic field line. The magnetic equator is at $h = 0$. (b) Forward- and (c) backward-propagating waves.

demonstrated that plasmaspheric hiss is a coherent emission with complex fine structure. Moreover, hiss was seen to be characterized by short-time discrete, rising tone, and falling tone elements, similar to but different from whistler-mode chorus emissions. In a subsequent analysis, Omura et al. (2015) showed that previously developed nonlinear growth theory of chorus waves (Omura & Nunn, 2011; Omura et al., 2008, 2009) could be adapted to apply to hiss. It was found that instantaneous wave amplitudes constructed from the observed plasmaspheric hiss waveforms from Van Allen Probe A favorably matched the theoretically predicted optimum wave amplitudes and threshold values. Nakamura et al. (2016) further tested the nonlinear wave growth theory applied to hiss emissions and found good agreement between the observed frequency sweep rates for rising tone elements and the nonlinear theory. In a complementary study, Nakamura et al. (2018) surveyed 3 years (2013–2015) of Van Allen Probes data on plasmaspheric plume crossing events and found that 97% of the observed plumes were accompanied by hiss emissions. Detailed examination of the hiss spectra showed that whistler-mode hiss in plasmaspheric plumes universally possesses fine structure of the type found by Summers et al. (2014) in the plasmasphere itself.

In this paper, we carry out self-consistent particle simulations of plasmaspheric hiss. We modify the electromagnetic simulation used for chorus wave generation studies (Hikishima & Omura, 2012; Hikishima et al., 2009a, 2010) to plasmaspheric conditions. As we shall show below, our simulation can reproduce very well the observed fine structure of plasmaspheric hiss reported above. In the following section, we describe the simulation method in detail. In section 3, we report the results, and in section 4, we provide discussion and state our conclusions.

2. Simulation Method

We perform a self-consistent electromagnetic full-particle simulation to study wave-particle interaction generating whistler-mode waves in the Earth's inner magnetosphere using a code originally developed by (Hikishima et al., 2009a, 2009b). The simulation system is a one-dimensional model taken along the ambient magnetic field near the equator of the Earth's dipole magnetic field. The ambient magnetic field line takes a nonuniform dipole field near the equatorial region, which is represented by a parabolic function $B = B_0(1+ah^2)$, where h is the distance along the field line and B_0 is the magnitude of the ambient magnetic

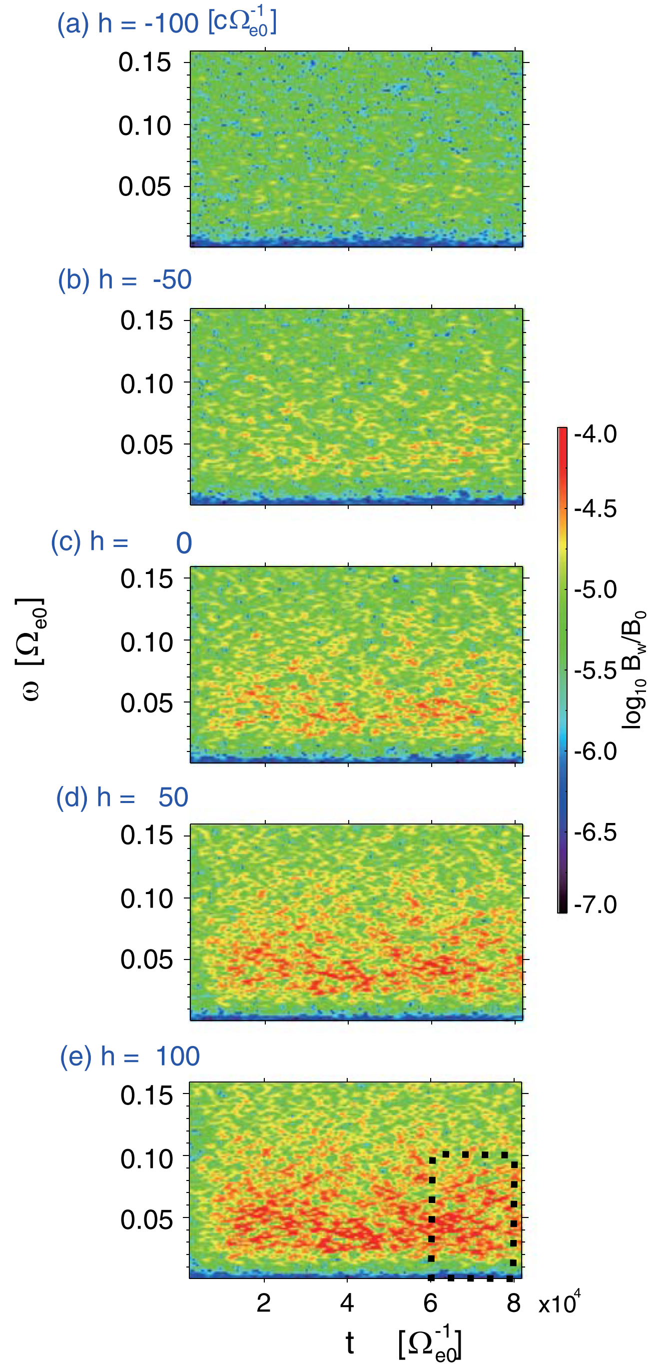

Figure 2. (a–e) Frequency-time spectrograms of transverse wave magnetic field B_w for forward-propagating waves at different locations $h = -100, -50, 0, 50, 100\ c\Omega_{e0}^{-1}$, over the time period $t = 0\text{–}8 \times 10^4\ \Omega_{e0}^{-1}$ in Figure 1. The dotted box in panel (e) at $h = 100\ c\Omega_{e0}^{-1}$ is plotted with different resolution in Figure 3.

field at the equator ($h = 0$). The parabolic coefficient takes the term $a = 1.86 \times 10^{-7}(c^{-1}\Omega_{e0})^2$, where c is the speed of light and Ω_{e0} is the equatorial electron gyrofrequency, representing a realistic curvature of the Earth's dipole field in the plasmasphere at $L = 4$.

Solving Maxwell's equations, we follow generation of whistler-mode waves with transverse wave field propagating parallel to the ambient magnetic field and neglect the parallel electric field to prevent a nonphysical diffusion of particles by enhanced electrostatic thermal fluctuations. The open boundary system allows the outgoing whistler-mode waves to be smoothly absorbed by applying a damping function at both edges of the simulation system. We solve the dynamics of both cold electrons and energetic electrons in the system. The energetic electrons are constructed as a loss cone distribution based on an anisotropic bi-Maxwellian. The parallel and perpendicular thermal velocities $v_{th\parallel} = 0.23c$ and $v_{th\perp} = 0.36c$ of energetic electrons yield an anisotropy $A = 1.4$. The plasma frequency ω_{pe}, which is a key parameter identifying the plasmasphere, takes a constant value $\omega_{pe} = 15\ \Omega_{e0}$ (plasma frequency 200 kHz with plasma density 500 cm^{-3}) along the magnetic field line.

The density ratio of energetic electrons to cold electrons is chosen as $N_h/N_c = 4 \times 10^{-4}$. All particles in the simulation are subject to a mirror force provided by the dipole magnetic field and bounce at the mirror points. Particles inside the loss cone at both boundaries of the simulation system are removed from the system because such particles eventually penetrate into the atmosphere. Particles outside the loss cone at the boundaries are reinjected into the simulation system, keeping the kinetic energies and pitch angles unchanged (Hikishima et al., 2010).

3. Results

3.1. Generation of Hiss Emissions

In Figure 1a, we plot frequency spectrograms of the transverse magnetic wave field B_w at different locations $h = -100, -50, 0, 50, 100\ c\Omega_{e0}^{-1}$ along the field line. The overall time interval of the power spectrograms corresponds to 10 s at $L = 4$. The field data are stored over a time interval $\Delta t = 2.05\ \Omega_{e0}^{-1}$ in the simulation. We apply the fast Fourier transform (FFT) with a Hann window using 2,048 data points corresponding to a time duration 4,194 Ω_{e0}^{-1} (51.3 ms) in an FFT frame shifted by 65.5 Ω_{e0}^{-1} (0.8 ms) at each time interval Δt.

A long-time simulation run was performed, starting from the initial velocity distribution function of anisotropic energetic electrons. Short electromagnetic emissions are steadily generated. Since the wave frequency is below the electron cyclotron frequency Ω_{e0}, with an electron plasma frequency 15 Ω_{e0}, the electromagnetic fields comprise whistler-mode waves that can interact with energetic electrons.

Using the spatial helicity of whistler-mode waves, we can separate the waves into two groups propagating forward and backward along the ambient magnetic field, as plotted in Figures 1b and 1c. The banded waves are generated at the equatorial region through local cyclotron resonance with anisotropic energetic electrons. The growing wave spectrograms over the long time scale $8 \times 10^5\ \Omega_{e0}^{-1}$ show unstructured broadband emissions which are characterized as whistler-mode hiss emissions. The emissions exhibit a common feature of plasmaspheric hiss, that is, broadband waves at frequencies $\omega < 0.1\ \Omega_{e0}$ and with a sudden decrease of the wave power in the lower frequency part ($\omega < 0.02\ \Omega_{e0}$) (Bortnik et al., 2008; Nakamura et al., 2018; Summers

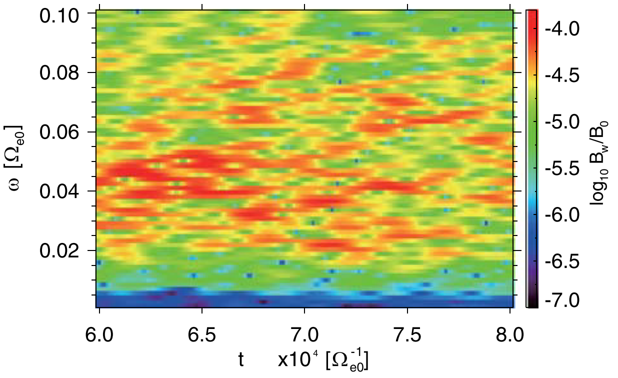

Figure 3. Enlarged frequency-time spectrogram ($t = 6 \times 10^4$ to $8 \times 10^4\ \Omega_{e0}^{-1}$, $\omega < 0.1\Omega_{e0}$) for the forward waves, indicated by the dotted box in Figure 2e.

et al., 2014). The banded emissions have a peak intensity around $\omega = 0.03\ \Omega_{e0}$ corresponding to several tens of pT at $L = 4$ (Meredith et al., 2004; Thorne et al., 1973).

Over the whole region ($h = -100\sim100\ c\Omega_{e0}^{-1}$) around the equator, the banded structure of the waves is formed in the frequency range of $\omega < 0.1\ \Omega_{e0}$. Both forward and backward waves, after the separation of propagation direction, show that short narrow-band wave packets with rising and falling tone frequencies are generated around the equator. These wave packets are amplified through propagation from the equator to higher latitude by interacting with counterstreaming energetic electrons. This result indicates importantly that the source region of the plasmaspheric hiss emissions is the equatorial region.

Figure 2 shows that the initial wave growth stage ($t = 0$–$8 \times 10^4\ \Omega_{e0}^{-1}$) of waves propagating forward in Figure 1 corresponds to time duration of 1 s. By comparing the spectrograms monitored at different locations $h = -100, -50, 0, 50, 100\ c\Omega_{e0}^{-1}$ along the magnetic field line, we find that the waves grow near the magnetic equator within a short distance. The substantial difference in wave amplitudes at locations $h = 0$ and $h = 50$ in Figure 2 is due to a large convective wave growth rate. The same wave growth process is found in the backward waves, as we see in Figure 1.

Further, we find enhanced wave amplitudes around $\omega = 0.05\ \Omega_{e0}$. These waves undergo convective wave growth during propagation toward higher latitude, and the frequency band becomes wider. Each of the wave packets is due to a nonlinear process under a coherent wave packet with a frequency variation. These wave packets with rising and falling tones form fine structures growing in space as shown in Figure 2.

3.2. Fine Structure of Hiss Emissions

In Figure 3, we have enlarged the dynamic wave spectrogram, modifying the resolution of the spectrogram (see the dotted box in Figure 2e). The sampling time of the field data is $\Delta t = 4.10\ \Omega_{e0}^{-1}$. We apply an FFT with the Hann window using 1,024 data points corresponding to a time duration 4,194 Ω_{e0}^{-1} (51.3 ms) in an FFT frame, and the frame is shifted by 131 Ω_{e0}^{-1} (1.6 ms). The simulation is started from the initial thermal noise determined by the initial distribution of energetic and cold electrons. The wave packets grow in a short time scale of $t = 1 \times 10^4\ \Omega_{e0}^{-1}$ corresponding to 0.12 s. We find elements of the waves grow with frequency variations resulting in fine structures in the dynamic spectrogram representative of the nonlinear wave growth process. This is essentially the same as the generation process of chorus wave emissions.

Figure 4 shows the space and time evolution of the wave amplitudes and frequencies of the transverse magnetic fields of the forward- and backward-traveling waves. Many wave packets forming lines with red colors in Figure 4a are formed, and they travel along the magnetic field with different group velocities, indicating wave packets are generated at many different frequencies of the broadband waves. Figure 4b shows the space-time evolution of the wave frequency determined from the phase variation of the transverse wave magnetic field with time step 4.10 Ω_{e0}^{-1}. The different fine colors indicate the wave generation processes take place at different frequencies. Frequencies of the wave packets are constant during their propagation, as indicated by the same colors in Figure 4b. The wave packets also undergo substantial convective growth as a result of propagation away from the magnetic equator. The lines with dark blue color in Figure 4b correspond to wave packets with frequencies $\omega \leq 0.1\ \Omega_{e0}$, and their wave amplitudes become larger in space and time through propagation as shown in Figure 4a.

Figure 5a presents an averaged amplitude of the transverse magnetic wave field B_w in the equatorial region $-20 < h < 20\quad [c\Omega_{e0}^{-1}]$. Wave packets are excited near the equator through cyclotron resonance. Figure 5b is the initial stage ($t = 0$–$1 \times 10^4\ \Omega_{e0}^{-1}$) of the simulation. The blue and red

lines represent temporal evolution of theoretical wave amplitudes calculated from linear wave growth rates (plotted in Figure 6) at $\omega = 0.03\ \Omega_{e0}$ and $0.06\ \Omega_{e0}$. These frequencies are chosen with reference to the maximum linear growth rate which occurs at $\omega = 0.06\ \Omega_{e0}$. After initiation of the simulation run,

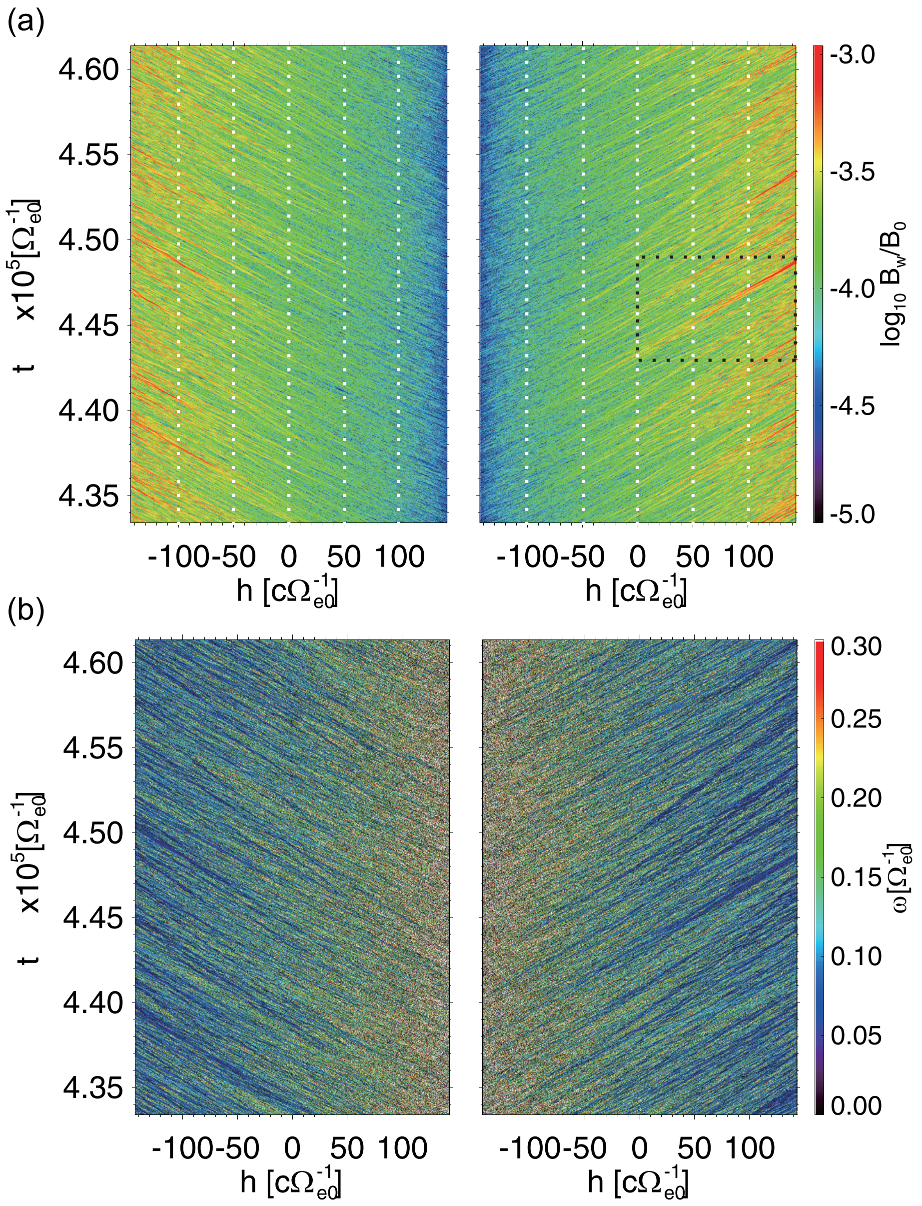

Figure 4. Space and time evolutions ($t = 4.3 \times 10^5$ to 4.6×10^5 Ω_{e0}^{-1}) of (a) wave amplitudes and (b) frequencies of forward- and backward-propagating waves plotted in the right and left panels, respectively. The location $h = 0$ corresponds to the magnetic equator. The area surrounded by the black dotted box is further analyzed in Figure 7. The white dotted lines are locations $h = -100, -50, 0, 50, 100\ c\Omega_{e0}^{-1}$ along the field line.

whistler-mode waves around the equator grow from a thermal fluctuation of the anisotropic energetic electrons following an amplification consistent with the linear wave growth rate up to $t = 0.2 \times 10^4\ \Omega_{e0}^{-1}$. The wave growth after $t = 0.2 \times 10^4\ \Omega_{e0}^{-1}$ is nonlinear because the wave spectra develop fine structures with large amplitudes, as shown in Figure 2. Each of the fine structures grows at the nonlinear growth rate which is greater than the linear growth rate, as shown in Figure 6. The wave amplitude in Figure 5 shows much smaller growth, because it is calculated by averaging the wave amplitudes in the equatorial region ($-20 < h < 20\ \ [c\Omega_{e0}^{-1}]$), while the fast growing wave packets are much localized in space and their contribution to the averaged value is limited.

We plot the linear wave growth rate and the nonlinear wave growth rates at the threshold and optimum wave amplitudes as function of wave frequency. Above the threshold wave amplitude, waves can grow at

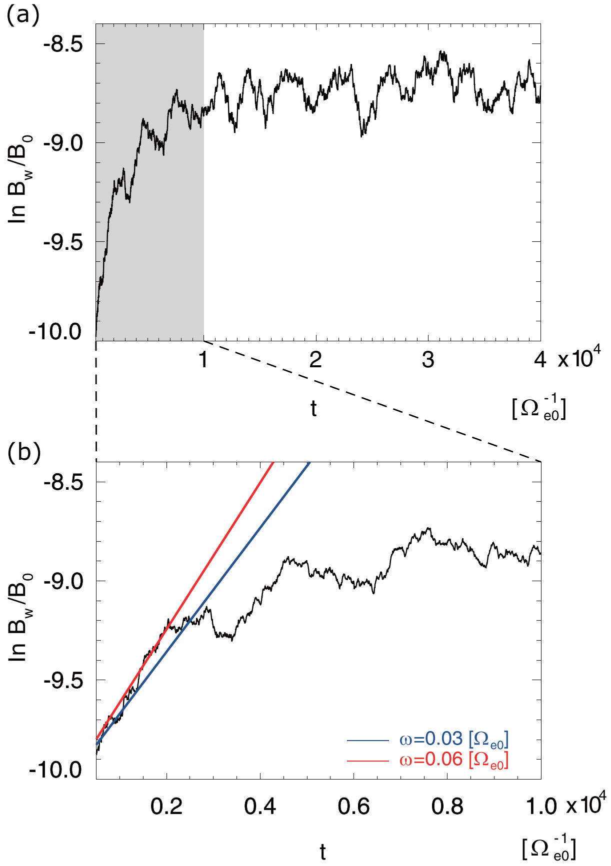

Figure 5. (a) Temporal evolution of the averaged transverse magnetic wave amplitude (natural logarithm scale) around the equator ($-20<h<20$ [$c\Omega_{e0}^{-1}$]). The shaded area is shown in panel (b). (b) The initial stage ($t = 0\text{–}1 \times 10^4\ \Omega_{e0}^{-1}$) of wave growth from thermal fluctuations. The blue and red lines show the wave amplitude calculated from theoretical linear wave growth rates at $\omega = 0.03\ \Omega_{e0}$ and $0.06\ \Omega_{e0}$, respectively.

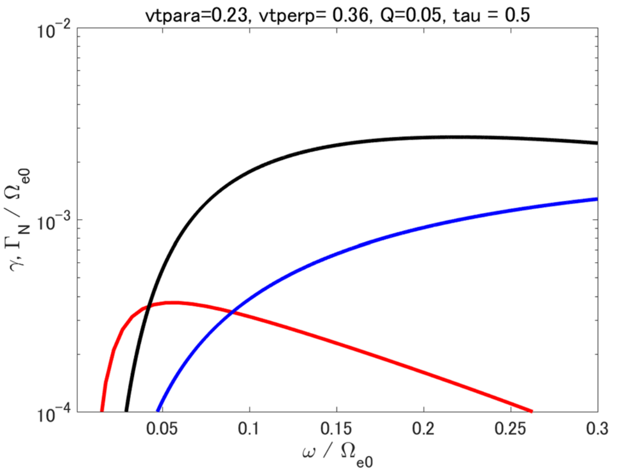

Figure 6. (Red) linear wave growth rate γ/Ω_{e0}, (black) nonlinear wave growth rate Γ_N/Ω_{e0} evaluated from the threshold amplitude, and (blue) nonlinear wave growth rate evaluated from the optimum amplitude as functions of wave frequency.

a fixed position near the equator as an absolute instability (Omura et al., 2009). While a wave above the threshold amplitude grows with a varying frequency, the wave amplitude cannot exceed much above the optimum amplitude, which satisfies the condition for the most efficient energy transfer from resonant electrons moving around the nonlinear trapping wave potential (Omura & Nunn, 2011). The linear wave growth rate is computed by Kyoto University Plasma Dispersion Analysis Package (KUPDAP) (Sugiyama et al., 2015) based on the plasma parameters of the simulation run listed in Table 1. Interestingly, the linear growth rate has a peak in the frequency at $\omega \sim 0.05\ \Omega_{e0}$ which depends on plasma parameters, while the nonlinear wave growth is larger than the linear wave growth in the higher frequency range.

We have extracted one of the hiss elements undergoing convective growth by choosing a frame of reference moving with the group velocity of the hiss element, as shown in Figure 7a. We calculated average values of the wave amplitude and instantaneous frequency of the wave packet by taking a short time window $\Delta t = 100\ \Omega_{e0}^{-1}$. The instantaneous frequency is the averaged value of frequencies calculated from a phase variation of dominant wave amplitudes within the time window Δt. As shown in Figures 7b and 7c, the frequency of the wave packet is nearly constant, while the amplitude increases gradually as the wave packet moves away from the equator. While the wave amplitude increases linearly as a function of distance from the equator, the gradient of the parabolic magnetic field also increases linearly. The inhomogeneity factor S (Equation 10 in Omura et al., 2009), comprising the major term containing the gradient of the magnetic field divided by the wave amplitude, can maintain the optimum value -0.4 for wave growth. As we find in Figure 7b, the convective wave growth subsides when the flux of the resonant electrons decreases. This is due to the adiabatic variation of the electron flux to smaller values of the parallel velocities as well as the shift of the resonance velocity to a larger value at a larger distance from the equator. From the spatial variation of B_w of the growing wave packet over $h = 50\sim100\ c\Omega_{e0}^{-1}$ shown in Figure 7b and from the group velocity $V_g = 0.05\,c$ evaluated from Figure 7a, we can calculate the temporal growth rate as $\Gamma_N = 0.7 \times 10^{-3}$, which is in good agreement with the nonlinear growth rate plotted in Figure 6. The maximum amplitude of the wave packets varies in a range of 80–200 pT depending on a distance from the equator as shown in Figure 7b.

To study the dependency of the wave packet amplitude on the wave frequency, we apply a band-pass filter with a frequency width of $0.01\ \Omega_{e0}$ to a time sequence ($t = 0\text{–}8 \times 10^{-4}\ \Omega_{e0}^{-1}$) of the wave field values observed at the equator. After applying the band-pass filter, we produce a waveform at each bin of the frequency band by taking an inverse FFT. We plot the instantaneous frequency calculated from a time variation of the transverse wave magnetic fields B_w and the instantaneous wave amplitude by each dot in Figure 8a. We plot the theoretical optimum and threshold amplitudes in Figure 8b. By changing the parameter Q, which is the depth of the electron hole formed by the coherent potentials of the hiss emissions (Omura et al., 2008), we found that the profile of the optimum and threshold wave amplitudes shows reasonable agreement with $Q = 0.05$. As shown in Figures 1 and 2, the wave in a range of $\omega > 0.1\Omega_{e0}$ contains thermal fluctuations. Because of the limited number of super particles in the simulation, the wave amplitude does not agree with the optimum amplitude in the higher frequency range $\omega \geq 0.1\ \Omega_{e0}$.

Table 1
Simulation Parameters

Parameter	Value
Time step:	$0.004\,\Omega_{e0}^{-1}$
Grid spacing:	$0.01\,c\Omega_{e0}^{-1}$
Plasma frequency of cold electrons: ω_{pe}	$15\,\Omega_{e0}$
Density ratio of hot electrons to cold electrons: N_h/N_c	4×10^{-4}
Total number of cold electrons	33,554,432
Total number of energetic electrons	67,108,864
Coefficient of parabolic magnetic field: a	$1.86\times10^{-7}\,(c^{-1}\Omega_{e0})^2$
Thermal velocity of hot electrons at the equator: $v_{th\parallel}, v_{th\perp}$	$0.23\,c$, $0.36\,c$

3.3. Precipitation of Resonant Electrons

Figure 9 shows the velocity distribution function $f(v_{\parallel}, v_{\perp})$ of the energetic electrons near the magnetic equator ($h \sim 0\,c\Omega_{e0}^{-1}$) plotted at different times ($t = 0, 0.5\times10^5$, 1.0×10^5, and $5.9\times10^5\ \Omega_{e0}^{-1}$). The initial velocity distribution ($t = 0\ \Omega_{e0}^{-1}$) is a subtracted bi-Maxwellian forming the loss cone with the typical size of $L = 4$. Energetic particles are in resonance with hiss elements at a wide range of resonance velocities of both forward- and backward-propagating waves. In Figure 9, energetic electrons with a positive parallel velocity ($v_{\parallel}$) are shown, which are caused by backward-propagating hiss waves. The hiss waves transport energetic electrons over the range $v_{\parallel} = 0.1{-}0.5\,c$ into the loss cone indicated by the white dashed line. The corresponding energy of the electrons is 2.5–80 keV. The present simulation result demonstrates that hiss waves with wave frequency $\omega < 0.1\,\Omega_{e0}$ can scatter electrons of tens of keV energy into the loss cone in a plasma environment with the cold plasma frequency $\omega_{pe} = 15\,\Omega_{e0}$.

4. Summary and Discussion

We have performed a self-consistent electromagnetic full particle simulation around the magnetic equator with a dipole field which is approximated by a parabolic function. In order to reproduce plasmaspheric hiss emissions, we set up anisotropic energetic electrons that resonate with whistler-mode waves assuming plasmaspheric parameters. The simulation shows that wave packets are generated through linear and nonlinear interactions with anisotropic energetic electrons that then propagate away from the equator by means of convective growth. The fine structures span a broadband within $\omega < 0.1\,\Omega_{e0}$, which is typical of hiss emissions observed by many satellites. The spectra of the hiss emissions show a frequency variation containing rising and falling tones, characteristic of nonlinear wave growth. The coherent hiss emissions resonate with energetic electrons and scatter them into the loss cone.

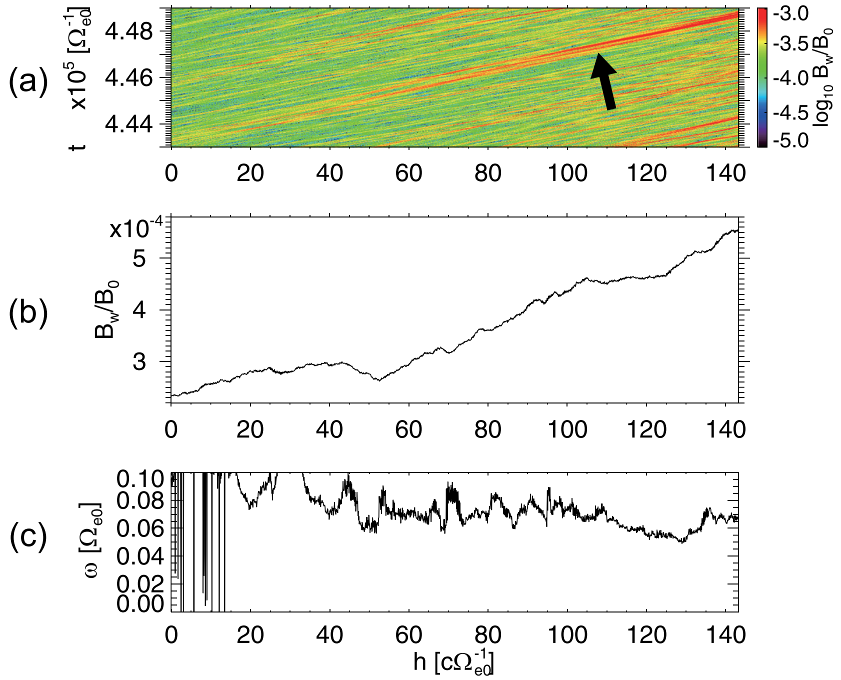

Figure 7. (a) Enlarged view of time-space evolution of transverse wave magnetic field B_w indicated by the dotted box in Figure 4a. Spatial profiles of (b) wave amplitude (c) averaged frequency of the wave packet indicated by the arrow.

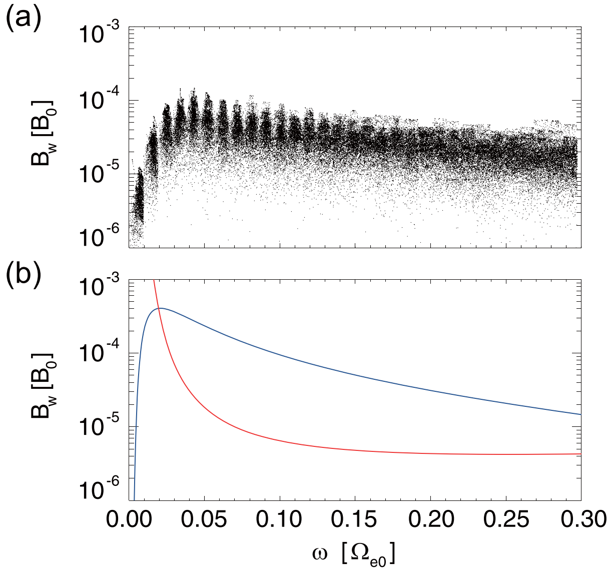

Figure 8. (a) Amplitudes and instantaneous frequencies of forward-traveling hiss waves at the equator. These are calculated from waveforms obtained by IFFT after applying a band-pass filter with width $\Delta\omega = 0.01\ \Omega_{e0}$ in the wave frequency spectrum at the equator over the interval $t = 0\text{–}8 \times 10^4\ \Omega_{e0}^{-1}$. (b) The threshold wave amplitude and optimum amplitude with parameters $\tau = 0.5$ and $Q = 0.05$ plotted in red and blue, respectively.

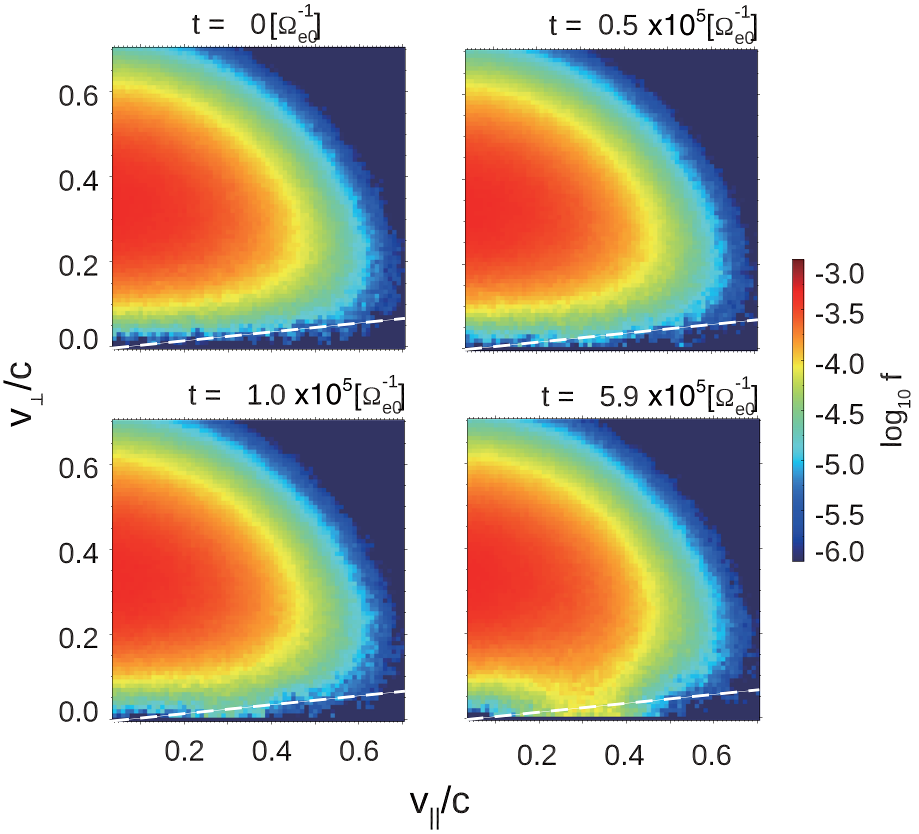

Figure 9. Velocity distribution function $f(v_{||},v_\perp)$ of energetic electrons near the equator at the times $t = 0$, 0.5×10^5, 1.0×10^5, and $5.9 \times 10^5\ \Omega_{e0}^{-1}$. The white dashed lines indicate the loss cone angle.

Even with modest temperature anisotropy ($A \sim 1.4$), which gives relatively small linear growth rates, efficient scattering of energetic electrons to lower pitch angles takes place near the equator, transferring kinetic energy to electromagnetic wave energy. This typifies nonlinear coherent wave-particle interaction. Because of the wide band spectra, the resonance velocity varies over a wide range, and electrons at many different pitch angles can be in resonance with the hiss waves. Multiple coherent interactions can take place at different pitch angles, effectively transferring the energetic electrons to lower pitch angles and precipitating the energetic electrons into the loss cone.

In the present simulation, we assume energetic electrons with a given temperature anisotropy as an initial condition, and an additional fresh energy source is not provided. However, in practice, energetic electrons are continuously transported into the plasmapause owing to the dawn-to-dusk electric field. The injected electrons into the equatorial region contribute to continuous generation of hiss emissions. A more realistic simulation model with continuous injection of energetic electrons would futher improve our understanding of the characteristics of hiss emissions.

Acknowledgments

The simulation data used in this paper are obtained from KEMPO1 code (http://space.rish.kyoto-u.ac.jp/software/) with minor modification applying Equation 1 in Hikishima et al. (2009a). The computer simulation was performed on the KDK computer system at the Research Institute for Sustainable Humanosphere, Kyoto University. This work was supported by JSPS KAKENHI Grant 17H06140. D. S. acknowledges support from a Discovery Grant of the Natural Sciences and Engineering Research Council of Canada.

References

Bortnik, J., Thorne, R. M., & Meredith, N. P. (2008). The unexpected origin of plasmaspheric hiss from discrete chorus emissions. *Nature*, *452*(7183), 62–66. https://doi.org/10.1038/nature06741

Breneman, A. W., Halford, A., Millan, R., McCarthy, M., Fennell, J., Sample, J., et al. (2015). Global-scale coherence modulation of radiation-belt electron loss from plasmaspheric hiss. *Nature*, *523*(7559), 193–195. https://doi.org/10.1038/nature14515

Cornilleau-Wehrlin, N., Solomon, J., Korth, A., & Kremser, G. (1993). Generation mechanism of plasmaspheric ELF/VLF hiss: A statistical study from GEOS 1 data. *Journal of Geophysical Research*, *98*(A12), 21,471–21,479. https://doi.org/10.1029/93JA01919

Green, J. L., Boardsen, S., Garcia, L., Taylor, W. W. L., Fung, S. F., & Reinisch, B. W. (2005). On the origin of whistler mode radiation in the plasmasphere. *Journal of Geophysical Research*, *110*, A03201. https://doi.org/10.1029/2004JA010495

Hartley, D. P., Kletzing, C. A., Chen, L., Horne, R. B., & Santolík, O. (2019). Van Allen Probes observations of chorus wave vector orientations: Implications for the chorus-to-hiss mechanism. *Geophysical Research Letters*, *46*, 2337–2346. https://doi.org/10.1029/2019GL082111

Hartley, D. P., Kletzing, C. A., Santolík, O., Chen, L., & Horne, R. B. (2018). Statistical properties of plasmaspheric hiss from Van Allen Probes observations. *Journal of Geophysical Research: Space Physics*, *123*, 2605–2619. https://doi.org/10.1002/2017JA024593

He, Z., Chen, L., Liu, X., Zhu, H., Liu, S., Gao, Z., & Cao, Y. (2019). Local generation of high-frequency plasmaspheric hiss observed by Van Allen Probes. *Geophysical Research Letters*, *46*, 1141–1148. https://doi.org/10.1029/2018GL081578

Hikishima, M., & Omura, Y. (2012). Particle simulations of whistler-mode rising-tone emissions triggered by waves with different amplitudes. *Journal of Geophysical Research*, *117*, A04226. https://doi.org/10.1029/2011JA017428

Hikishima, M., Omura, Y., & Summers, D. (2010). Microburst precipitation of energetic electrons associated with chorus wave generation. *Geophysical Research Letters*, *37*, L07103. https://doi.org/10.1029/2010GL042678

Hikishima, M., Yagitani, S., Omura, Y., & Nagano, I. (2009a). Full particle simulation of whistler-mode rising chorus emissions in the magnetosphere. *Journal of Geophysical Research*, *114*, A01203. https://doi.org/10.1029/2008JA013625

Hikishima, M., Yagitani, S., Omura, Y., & Nagano, I. (2009b). Coherent nonlinear scattering of energetic electrons in the process of whistler mode chorus generation. *Journal of Geophysical Research*, *114*, A10205. https://doi.org/10.1029/2009JA014371

Kennel, C. F., & Petschek, H. E. (1966). Limit on stably trapped particle fluxes. *Journal of Geophysical Research*, *71*(1), 1–28. https://doi.org/10.1029/JZ071i001p00001

Kennel, C. F., & Thorne, R. M. (1967). Unstable growth of unducted whistlers propagating at an angle to the geomagnetic field. *Journal of Geophysical Research*, *72*(3), 871–878. https://doi.org/10.1029/JZ072i003p00871

Kim, K.-C., & Shprits, Y. (2019). Statistical analysis of hiss waves in plasmaspheric plumes using Van Allen Probe observations. *Journal of Geophysical Research*, *124*, 1904–1915. https://doi.org/10.1029/2018JA026458

Kletzing, C., Bounds, W. S., Hospodarsky, S. R., Santolik, G. B., Wygant, O., Bonnell, J. R., et al. (2014). Evidence for significant local generation of plasmaspheric hiss, Abstract SM 14A-09 presented at the 2014 AGU Fall Meeting, San Francisco, CA December 15–19.

Li, W., Thorne, R. M., Bortnik, J., Reeves, G. D., Kletzing, C. A., Kurth, W. S., et al. (2013). An unusual enhancement of low-frequency plasmaspheric hiss in the outer plasmasphere associated with substorm-injected electrons. *Geophysical Research Letters*, *40*, 3798–3803. https://doi.org/10.1002/grl.50787

Li, W., Ni, B., Thorne, R. M., Bortnik, J., Nishimura, Y., Green, J. C., et al. (2014). Quantifying hiss-driven energetic electron precipitation: A detailed conjunction event analysis. *Geophysical Research Letters*, *41*, 1085–1092. https://doi.org/10.1002/2013GL059132

Liu, N., Su, Z., Gao, Z., Zheng, H., Wang, Y., Wang, S., et al. (2020). Comprehensive observations of substorm-enhanced plasmaspheric hiss generation, propagation, and dissipation. *Geophysical Research Letters*, *47*, e2019GL086040. https://doi.org/10.1029/2019GL086040

Lyons, L. R., & Thorne, R. M. (1973). Equilibrium structure of radiation belt electrons. *Journal of Geophysical Research*, *78*(13), 2142–2149. https://doi.org/10.1029/JA078i013p02142

Lyons, L. R., Thorne, R. M., & Kennel, C. F. (1972). Pitch-angle diffusion of radiation belt electrons within the plasmasphere. *Journal of Geophysical Research*, *77*(19), 3455–3474. https://doi.org/10.1029/JA077i019p03455

Malaspina, D. M., Jaynes, A. N., Hospodarsky, G., Bortnik, J., Ergun, R. E., & Wygant, J. (2017). Statistical properties of low-frequency plasmaspheric hiss. *Journal of Geophysical Research: Space Physics*, *122*, 8340–8352. https://doi.org/10.1002/2017JA024328

Meredith, N. P., Horne, R. B., Glauert, S. A., Thorne, R. M., Summers, D., Albert, J. M., & Anderson, R. R. (2006). Energetic outer zone electron loss timescales during low geomagnetic activity. *Journal of Geophysical Research*, *111*, A05212. https://doi.org/10.1029/2005JA011516

Meredith, N. P., Horne, R. B., Kersten, T., Li, W., Bortnik, J., Sicard, A., & Yearby, K. H. (2018). Global model of plasmaspheric hiss from multiple satellite observations. *Journal of Geophysical Research: Space Physics*, *123*, 4526–4541. https://doi.org/10.1029/2018JA025226

Meredith, N. P., Horne, R. B., Thorne, R. M., Summers, D., & Anderson, R. R. (2004). Substorm dependence of plasmaspheric hiss. *Journal of Geophysical Research*, *109*, A06209. https://doi.org/10.1029/2004JA010387

Nakamura, S., Omura, Y., & Summers, D. (2018). Fine structure of whistler mode hiss in plasmaspheric plumes observed by the Van Allen Probes. *Journal of Geophysical Research: Space Physics*, *123*, 9055–9064. https://doi.org/10.1029/2018JA025803

Nakamura, S., Omura, Y., Summers, D., & Kletzing, C. A. (2016). Observational evidence of the nonlinear wave growth theory of plasmaspheric hiss. *Geophysical Research Letters*, *43*, 10,040–10,049. https://doi.org/10.1002/2016GL070333

Ni, B., Li, W., Thorne, R. M., Bortnik, J., Ma, Q., Chen, L., et al. (2014). Resonant scattering of energetic electrons by unusual low-frequency hiss. *Geophysical Research Letters*, *41*, 1854–1861. https://doi.org/10.1002/2014GL059389

Omura, Y., Hikishima, M., Katoh, Y., Summers, D., & Yagitani, S. (2009). Nonlinear mechanisms of lower-band and upper-band VLF chorus emissions in the magnetosphere. *Journal of Geophysical Research*, *114*, A07217. https://doi.org/10.1029/2009JA014206

Omura, Y., Katoh, Y., & Summers, D. (2008). Theory and simulation of the generation of whistler-mode chorus. *Journal of Geophysical Research*, *113*, A04223. https://doi.org/10.1029/2007JA012622,.

Omura, Y., Nakamura, S., Kletzing, C. A., Summers, D., & Hikishima, M. (2015). Nonlinear wave growth theory of coherent hiss emissions in the plasmasphere. *Journal of Geophysical Research: Space Physics*, *120*, 7642–7657. https://doi.org/10.1002/2015JA021520

Omura, Y., & Nunn, D. (2011). Triggering process of whistler mode chorus emissions in the magnetosphere. *Journal of Geophysical Research*, *116*, A05205. https://doi.org/10.1029/2010JA016280

Smith, E. J., Frandsen, A. M. A., Tsurutani, B. T., Thorne, R. M., & Chan, K. W. (1974). Plasmaspheric hiss intensity variations during magnetic storms. *Journal of Geophysical Research*, *79*(16), 2507–2510. https://doi.org/10.1029/JA079i016p02507

Su, Z., Liu, N., Zheng, H., Wang, Y., & Wang, S. (2018). Multipoint observations of nightside plasmaspheric hiss generated by substorm-injected electrons. *Geophysical Research Letters*, *45*, 10,921–10,932. https://doi.org/10.1029/2018GL079927

Sugiyama, H., Singh, S., Omura, Y., Shoji, M., Nunn, D., & Summers, D. (2015). Electromagnetic ion cyclotron waves in the Earth's magnetosphere with a kappa-Maxwellian particle distribution. *Journal of Geophysical Research: Space Physics*, *120*, 8426–8439. https://doi.org/10.1002/2015JA021346

Summers, D., Ni, B., & Meredith, N. P. (2007a). Timescales for radiation belt electron acceleration and loss due to resonant wave-particle interactions: 1. Theory. *Journal of Geophysical Research*, *112*, A04206. https://doi.org/10.1029/2006JA011801

Summers, D., Ni, B., & Meredith, N. P. (2007b). Timescales for radiation belt electron acceleration and loss due to resonant wave-particle interactions: 2. Evaluation for VLF chorus, ELF hiss, and electromagnetic ion cyclotron waves. *Journal of Geophysical Research*, *112*, A04207. https://doi.org/10.1029/2006JA011993

Summers, D., Ni, B., Meredith, N. P., Horne, R. B., Thorne, R. M., Moldwin, M. B., & Anderson, R. R. (2008). Electron scattering by whistler-mode ELF hiss in plasmaspheric plumes. *Journal of Geophysical Research*, *113*, A04219. https://doi.org/10.1029/2007JA012678

Summers, D., Omura, Y., Nakamura, S., & Kletzing, C. A. (2014). Fine structure of plasmaspheric hiss. *Journal of Geophysical Research: Space Physics*, *119*, 9134–9149. https://doi.org/10.1002/2014JA020437

Thorne, R., Church, S., & Gorney, D. (1979). On the origin of plasmaspheric hiss: The importance of wave propagation and the plasmapause. *Journal of Geophysical Research*, *84*(A9), 5241–5247. https://doi.org/10.1029/JA084iA09p05241

Thorne, R. M., Church, S. R., Malloy, W. J., & Tsurutani, B. T. (1977). The local time variation of ELF emissions during periods of substorm activity. *Journal of Geophysical Research*, *82*(10), 1585–1590. https://doi.org/10.1029/JA082i010p01585

Thorne, R. M., Li, W., Ni, B., Ma, Q., Bortnik, J., Baker, D. N., et al. (2013). Evolution and slow decay of an unusual narrow ring of relativistic electrons near L ∼3.2 following the September 2012 magnetic storm. *Geophysical Research Letters*, *40*, 3507–3511. https://doi.org/10.1002/grl.50627

Thorne, R. M., Smith, E. J., Burton, R. K., & Holzer, R. E. (1973). Plasmaspheric hiss. *Journal of Geophysical Research*, *78*(10), 1581–1596. https://doi.org/10.1029/JA078i010p01581

Thorne, R. M., Smith, E. J., Fiske, K. J., & Church, S. R. (1974). Intensity variation of ELF hiss and chorus during isolated substorms. *Geophysical Research Letters*, *1*, 193–196. https://doi.org/10.1029/GL001i005p00193

Tsurutani, B. T., Falkowski, B. J., Pickett, J. S., Santolik, O., & Lakhina, G. S. (2015). Plasmaspheric hiss properties: Observations from Polar. *Journal of Geophysical Research: Space Physics*, *120*, 414–431. https://doi.org/10.1002/2014JA020518

Tsurutani, B. T., Park, S. A., Falkowski, B. J., Lakhina, G. S., Pickett, J. S., Bortnik, J., et al. (2018). Plasmaspheric hiss: Coherent and intense. *Journal of Geophysical Research: Space Physics*, *123*, 10,009–10,029. https://doi.org/10.1029/2018JA025975

Tsurutani, B. T., Smith, E. J., & Thorne, R. M. (1975). Electromagnetic hiss and relativistic electron losses in the inner zone. *Journal of Geophysical Research*, *80*(4), 600–607. https://doi.org/10.1029/JA080i004p00600

Zhang, W., Fu, S., Gu, X., Ni, B., Xiang, Z., Summers, D., et al. (2018). Electron scattering by plasmaspheric hiss in a nightside plume. *Geophysical Research Letters*, *120*, 4618–4627. https://doi.org/10.1029/2018GL077212